Analytical-Numerical Model for Synchronous Homopolar Machines

Amedeo Vannini, Mauro Di Nardo, Alessandro Marfoli, Jacopo Riccio,
Mukhammed Murataliyev, Antonino La Rocca, and Chris Gerada

***Abstract*—Synchronous homopolar machines represent a viable solution for applications requiring a robust electro-mechanical conversion system. Their diffusion is hindered by the low power density and by their complex three-dimensional magnetic behavior which requires time-consuming 3D finite element analysis for the performance prediction. This manuscript proposes a general analytical electromagnetic model able to evaluate the performance of both split and pass-through winding layouts addressing the existing methodological gap of the literature. The modelling approach - based on equivalent winding and permeance functions - reduces the resolution of the 3D electromagnetic problem to two axially coupled 2D problems considering all the mmf contributions, including the end-winding one, which cannot be neglected for the split winding configuration. The analytical model is numerically implemented and its predictions are compared with the 3D FE analysis. The comparison demonstrates the effectiveness of the proposed model in estimating the performance in different operating conditions and any rotor position. Several experimental tests are carried out on a laboratory-scale prototype to validate the analytical predictions in terms of inductances vs. rotor position and voltage waveforms. Although the experimental assessment shows the limitation of the proposed technique, i.e. the linear magnetic behaviour, this could potentially serve as a basis for the fast design optimization of this machine topology.**

***Index Terms*—Analytical Model, Synchronous Homopolar Machine, Permeance Functions, Winding Function, Inductances, 3D FEA.**

NOMENCLATURE

α	relative rotor-stator angular position.
${}^kB_g$	total airgap flux density in the section k.
${}^kB_{g,0}$	airgap flux density in the section k due to the homopolar contribution.
${}^kB_{g,2D}$	airgap flux density in the section k due to the active sides.
${}^kB_{g,exc}$	airgap flux density in the section k due to the excitation coil contribution.
${}^kB_{g,EW}$	airgap flux density in the section k due to the end-winding contribution.
C_E	electromagnetic coenergy.
ε_g	airgap flux tubes length function.
ϕ_0	homopolar flux.
$\mathscr{F}_{RS,2D}$	rotor-stator magnetic voltage due to the armature field.
$\mathscr{F}_e$	equivalent airgap MMF.
$\mathscr{F}_{e,EW}$	equivalent end-winding MMF.
$\mathscr{F}_{RS,0}$	homopolar rotor-stator airgap magnetic tension.
γ	normalised coordinate mapping the tangential position along the airgap.
$\mathbf{L}$	inductance matrix.
ℓ	section stack length.
$\bar{i}$	current vector.
μ_0	vacuum permeability.
μ_e	equivalent permeability function.
$\bar{M}$	motional coefficient vector.
$\mathscr{M}_0$	homopolar MMF.
$\mathscr{M}_{2D}$	active sides' MMF.
ν	anisotropy function.
$\bar{N}$	vector of winding functions.
$\bar{N}_e$	winding function vector.
$\bar{N}_{e,EW}$	equivalent end-winding winding function vector.
N_{exc}	number of excitation coil turns.
n_{ph}	overall number of phases.
Ω_g	generalised cylinder where the Gauss' law is enforced.
$\bar{\Psi}$	linkage flux vector function.
$\mathbf{R}$	resistance matrix.
r_g	airgap magnetic-equipotential line function.
r_r	rotor magnetic-equipotential line function.
r_s	stator magnetic-equipotential line function.
${}^k\Sigma$	arbitrary cross-section where the magnetic fields are evaluated in the k section.
τ_g	medium magnetic-equipotential surface airgap function.
T_E	electromagnetic torque.
$\bar{v}$	phase voltage vector.
Ξ_g	generalised cylinder where the total Gauss' law is enforced.

I. INTRODUCTION

SYNCRHONOUS homopolar machines (SHMs), also known as homopolar inductor alternators, have been studied for many years and the first work dates back to the '60s [1]. Their appeal lies in the remarkably distinguishing feature of the stationary DC excitation which makes them an intriguing choice for several applications requiring a particularly robust electro-mechanical conversion system. Indeed, their simple rotor structure - PM-free and without any brush-slip system - makes them suitable for applications characterized by harsh environments or by the need of having zero no-load losses, e.g. flywheel. SHMs combine the controllability

A. Vannini, A. Marfoli, J. Riccio, M. Murataliyev, A. La Rocca, and C. Gerada are with the Power Electronics, Machines and Control (PEMC) Research Institute, University of Nottingham, Nottingham, NG7 2GT, UK. (email: amedeo.vannini2@nottingham.ac.uk)

M. Di Nardo is with the Department of Electrical Engineering and Information Technology, Politecnico di Bari, Bari, 70126 Italy (e-mail: mauro.dinardo@poliba.it)

of wound-field synchronous machines with robust rotor-like switched reluctance machines. Indeed, [2] proposes an elegant equivalence between SHMs and these two more common machine topologies. Notably, the absence of PMs not only mitigates risks related to high-temperature operation [3] but also guarantees stability in the face of possible shortages in rare-earth elements [4]. Additionally, the capability to control the excitation field allows for reliable de-excitation, with the option of reducing current to null conditions in case of failure. For these interesting aspects, SHMs have been studied for a wide variety of applications ranging from flywheels energy storage systems [5], marine and mining propulsion [6], [7], heavy traction [8], to aerospace power generation [9]. The other aspect making this particular machine topology really interesting for very high power density applications is related to its perfect adaptability to be used with high-temperature superconductors for the excitation coil. Indeed, being stationary and relatively simple, with respect to the classical multiphase winding of radial flux machine, the complex thermal management required by this technology is definitely easier [6], [10]. The regular alternating of the north and south magnetic poles along the tangential direction typical of the electrical machine is split between the two axial portions in SHMs, as seen in the elegant comparison between PMSMs and SHMs [11]. As a consequence, the active axial length is doubled, which halves the power density. A more comprehensive and interesting comparison with more conventional reluctance-based machine topologies is reported in [8] where it is shown that SHMs is a competitive machine topology when the application requires a very robust electromagnetic conversion system (e.g. the absence of slip-rings and PMs) and the excitation coil is intensively cooled allowing high current density.

A. Literature review

The prevailing configuration for SHMs comprises two identical laminated stator core sections equipped with armature windings, featuring a field winding located between them. The solenoid excitation coil provides the homopolar magnetization of the machine along an axial flux path within the solid ferromagnetic sleeves. The salient nature of the rotor enables the electromechanical conversion process. Various configurations have been proposed in the literature for this machine topology. Regarding the stator winding, two main layouts are predominantly considered, as illustrated in Fig. 1.

1) The pass-through armature configuration features armature coils that extend along the entire length of the machine crossing the mid-plane [5]. In this case, an angular shift between the two rotor pole sections is typically employed to achieve variable coupling between each armature phase and the field winding and thus non-zero average torque.
2) The split-armature configuration has armature coils that span just one of the two axial sections, with the coils being appropriately connected as necessary (e.g., [9], [12]). In this case, the angular shift between the two rotor sections is no longer necessary due to the presence of independent armature winding systems.

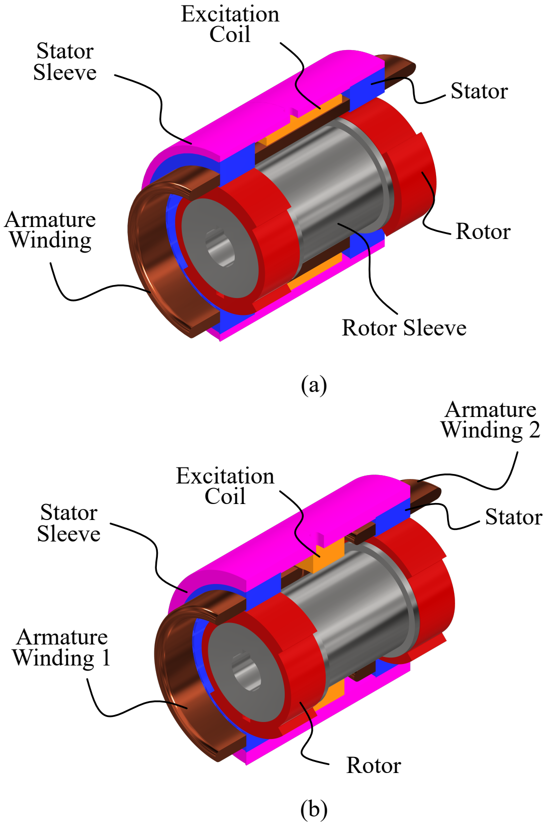

Fig. 1: Types of winding layouts for SHMs: (a) *pass-through armature* and (b) *split-armature*.

The pass-through armature option allows for more compact design solutions due to the absence of the end-windings in the central part. However, the reduced space available for hosting the excitation coil may pose additional challenges in managing its location between the stators. Thicker back-irons are needed to guarantee enough space allocation to the excitation coil, as shown in Fig. 1. The different shapes of the excitation coil can also be appreciated, with the same cross-section being considered. On the other hand, the split armature offers ease in manufacturing, improved integration of the excitation coil in the central part, and greater degrees of freedom for winding layout design, potentially enabling the realisation of fault-resilient solutions [9]. Indeed, this arrangement offers higher flexibility in the machine architecture permitting the creation of two separate winding systems [13]. Furthermore, guaranteeing the relative alignment between the two stators is no longer a challenge, allowing the adoption of conventional winding methods. Combinations of the two winding types have also been proposed for bearingless flywheel energy storage systems, where the employment of SHM is of particular interest due to its high efficiency during idling periods [5], [14], [15].

Due to the inherent 3D-field map distribution, the employment of 3D finite-element (FE) approaches for the design is necessary. Indeed, the main excitation flux tube has a 3D path which radially crosses the laminated salient rotor cores, then the airgap and the laminated stators and closes axially via the external and internal solid magnetic sleeves as shown qualitatively in Fig. 2 for the split-armature case; on the contrary, the armature flux has a more conventional path. The same figure also reports the no-load airgap flux density sampled in the middle of the two stator sections clearly showing the rationals behind the name of the machine, i.e. homopolar. Indeed, each stator section experiences a unidirectional magnetic flux and the two airgap flux density distributions are complementary.

3D FEA is highly accurate in estimating the machine performance but has a substantial computational burden, limiting its utilization in the design optimization process. Simplified 2D equivalent FE models offer a computationally efficient means for the design; however, this efficiency comes at the cost of reduced accuracy and an increased reliance on assumptions, especially in the case of electrical machines with a complex 3D flux path.In [2], the excitation field is simulated with virtual excitation windings for rotor pole shape optimization. Other equivalent 2D FE approaches incorporate the 3D magnetic field distribution into a 2D FE framework by adding an extra term to the equations of the vector magnetic potential through jump boundary conditions [16], [17]. Nevertheless, the latter has not been validated against a full 3D FE model. Furthermore, all the equivalent 2D FE techniques fall short when split-winding layouts are considered. Analytical modelling techniques based on airgap equivalent permeances, such as those proposed in [12], [18], [19], are still limited to pass-through winding layouts. Other prevalent analytical approaches involve complex 3D lumped parameter reluctance networks [5], [20], where 2D magnetic circuit slices are interconnected through axial reluctances. While capable of considering leakage fluxes and saturation phenomena, these approaches may result in large and complex equivalent networks. The split winding layout poses a further challenge to the electromagnetic modelling of this machine topology. Indeed, in this configuration, also the central end-winding part contributes to the main 3D flux path creation thus the respective end-winding magneto-motive force contribution has to be kept into account.

This paper presents a general approach for analysing the electromagnetic performance of SHMs equipped with any of two main winding layouts. The authors aim to close the gap in the available literature by proposing a computationally efficient yet accurate performance estimation methodology that can be used for sizing purposes. Indeed, this work focuses on the split-winding layout, being the most challenging, presenting a general modelling framework capable of accounting also for the end-windings mmf contribution without neglecting the position-dependent anisotropic behaviour. The general analytical model presented in [21] for the electromagnetic analysis of electrical machines is here applied and tailored for modelling SHMs. This modelling approach - based on equivalent winding function and permeance function - has been effectively used to model the most common electrical machine topologies, such as squirrel-cage induction motors [22], wound-field synchronous machines [23], and line-start PM synchronous motors [24]. Indeed, this method enables the rapid estimation of electromagnetic performance under linear magnetic operation, effectively capturing interactions between time and space harmonics, including the impact of stator and rotor anisotropies and winding layout distribution.

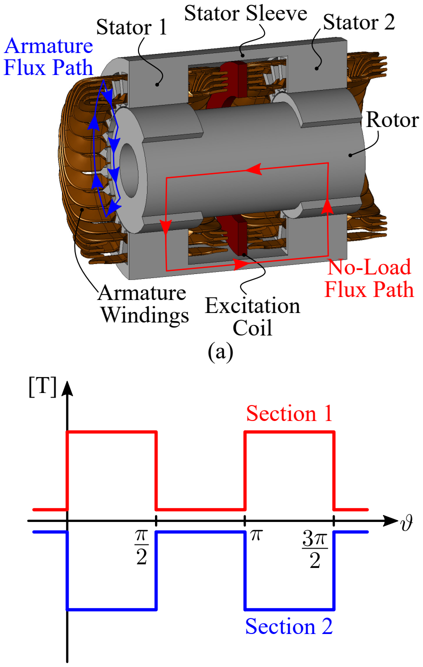

Fig. 2: a) Qualitative no-load and armature flux paths and b) no-load airgap flux density distribution for a split-armature SHM.

The manuscript first lays down the modelling assumptions and main formulation (Section II), then details the modelling technique by deriving the magneto-motive force (MMF) and the airgap flux density contributions of both armatures, excitation coil and end winding part (Section III). Once the airgap flux density is defined, the various flux linkages and then the matrix of inductances can be derived (Section IV). Section V describes the numerical implementation of the proposed model outlining the details of both winding function and permeance function. Section VI reports the performance estimation of the model in terms of the spatial distribution of the airgap flux density and inductance behaviour with the rotor position in different operating conditions. The accuracy of the proposed modelling technique is assessed by comparing the results first with a 3-D FEA and then with the experimental measurements carried out on a laboratory-scale prototype rated 1.2 kW (Section VII).

II. ASSUMPTIONS AND MODELLING FRAMEWORK

The peculiar structure of SHM featuring two machine sections and an axial excitation coil that are potentially magnetically coupled requires a modification of the adopted modelling framework [21], necessary to capture the main electromagnetic quantities. The modelling approach lies in the following hypotheses.

1) Straight extruded geometry along the machine rotating axis (i.e., no skewing) with the stator and rotor magnetic cores featuring equal length ℓ (see Fig. 3) much larger than the transversal size.
2) Negligible MMF drop, hysteresis losses, and eddy currents in the iron cores.

3) Negligible mutual influence between main and secondary field lines, enabling the separate analysis of principal and leakage fluxes.
4) The magnetic field variation in the airgap along the radial direction is negligible.

The voltage equation for the machine, featuring an overall number of phases denoted as n_{ph}, can be expressed in matrix form [22]:

$$\bar{v} = \mathbf{R} \cdot \bar{i} + \mathbf{L}(\alpha) \cdot \frac{d\bar{i}}{dt} + \bar{M}(\alpha, \bar{i}) \cdot \frac{d\alpha}{dt} \tag{1}$$

where $\mathbf{R} \in \mathbb{R}^{n_{ph} \times n_{ph}}$ is the resistance matrix, $\mathbf{L} \in \mathbb{R}^{n_{ph} \times n_{ph}}$ is the inductance matrix depending only on the variable α describing the relative rotor-stator position, and $\bar{M}(\alpha, \bar{i}) \in \mathbb{R}^{n_{ph} \times 1}$ the motional coefficient vector defined in (2).

$$\bar{M}(\alpha, \bar{i}) = \frac{d\mathbf{L}(\alpha)}{d\alpha} \cdot \bar{i} \tag{2}$$

The voltage and current vectors are defined, respectively, as:

$$\bar{i} = \begin{bmatrix} \bar{i}_1 \\ \bar{i}_2 \\ i_{exc} \end{bmatrix} \in \mathbb{R}^{n_{ph} \times 1}, \quad \bar{v} = \begin{bmatrix} \bar{v}_1 \\ \bar{v}_2 \\ v_{exc} \end{bmatrix} \in \mathbb{R}^{n_{ph} \times 1} \tag{3}$$

where the subscripts 1 and 2 refer to the vectors of sections 1 and 2, respectively, while ”exc” refers to the excitation coil. The electromagnetic torque T_E is then determined as the derivative of the electromagnetic coenergy $C_E(\alpha, \bar{i})$ with respect to α, obtaining [22]:

$$T_E(\alpha, \bar{i}) = \frac{\partial C_E(\alpha, \bar{i})}{\partial \alpha} = \frac{1}{2} \cdot \bar{i}^T \cdot \bar{M}(\alpha, \bar{i}) \tag{4}$$

The electromagnetic analysis can be focused only on the two main airgaps, which are magnetically interconnected by the rotor and stator sleeves, providing a low magnetic permeability path. Hence, the 3D electromagnetic problem can be reduced to the resolution of two axially-coupled equivalent quasi-2D problems by neglecting the axial component of the magnetic fields in the airgaps [2]. Additionally, considering the negligible variation of the flux density along the axis in the main airgap of each section (i.e., the z component), the analysis can focus on the resolution of the field at two arbitrary cross-sections (${}^1\Sigma$ and ${}^2\Sigma$) denoted as ${}^1B_g(\gamma, \alpha, \bar{i})$ for section 1 and ${}^2B_g(\gamma, \alpha, \bar{i})$ for section 2. Fig. 3 depicts the two planes ${}^1\Sigma$ and ${}^2\Sigma$ where the magnetic fields are evaluated. The coordinate γ represents the normalized tangential position along the airgap, mapping the interval $[0, 1)$. In the subsequent section, the solution to the electromagnetic problem under the aforementioned assumptions will be presented.

III. AIRGAP MAGNETIC FIELD CONTRIBUTIONS

The solution to the magnetic problem is obtained by applying the superposition principle, valid for magnetically linear problems. This principle allows the derivation of the total airgap flux density ${}^kB_g(\gamma, \alpha, \bar{i})$ in a generic section $k = 1, 2$ as follows:

$${}^kB_g(\gamma, \alpha, \bar{i}) = {}^kB_{g,2D}(\gamma, \alpha, \bar{i}) + {}^kB_{g,0}(\gamma, \alpha, \bar{i}) \tag{5}$$

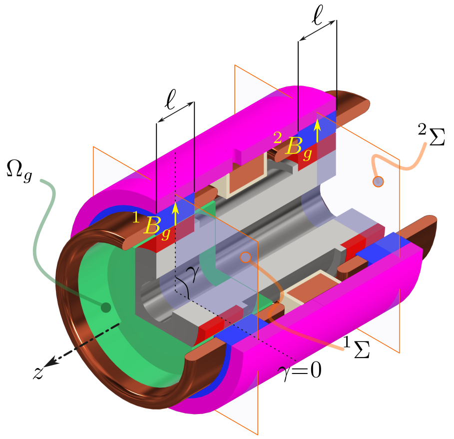

Fig. 3: View of the SHM with the reference planes ${}^1\Sigma$ and ${}^2\Sigma$.

The first component, ${}^kB_{g,2D}(\gamma, \alpha, \bar{i})$, represents the magnetic field resulting from the MMF contribution of the active sides within the machine cross-section. This corresponds to the conventional solution of the 2D problem for long-drum type machines as addressed in [21]. The second component, ${}^kB_{g,0}(\gamma, \alpha, \bar{i})$, is unique to homopolar-type machines and it is due to homopolar field contributions. It is due to both excitation coil and end-windings MMFs, where the latter is present only in the case of split-winding arrangements:

$${}^kB_{g,0}(\gamma, \alpha, \bar{i}) = {}^kB_{g,exc}(\gamma, \alpha, \bar{i}) + {}^kB_{g,EW}(\gamma, \alpha, \bar{i}) \tag{6}$$

where ${}^kB_{g,exc}(\gamma, \alpha, \bar{i})$ and ${}^kB_{g,EW}(\gamma, \alpha, \bar{i})$ are the contribution to the flux densities of the excitation coil and the end-windings, respectively. In the following three subsections, the various components contributing to the airgap flux density will be derived.

A. Armature field

The airgap flux density related to the armature field contribution can be determined with an approach similar to switched reluctance-type machines. Due to the geometrical symmetry assumed for the two sections, the airgap flux density distribution is the same resulting in ${}^1B_{g,2D}(\gamma, \alpha, \bar{i}) = {}^2B_{g,2D}(\gamma, \alpha, \bar{i})$. For the sake of compactness, the section's apex k will not be reported in this subsection. The airgap flux density function can be written as:

$$B_{g,2D}(\gamma, \alpha, \bar{i}) = \frac{\mu_0}{\varepsilon_g(\gamma, \alpha)} \cdot \mathscr{F}_{RS,2D}(\gamma, \bar{i}, \alpha) \tag{7}$$

where μ_0 is the vacuum permeability, $\mathscr{F}_{RS,2D}(\gamma, \bar{i}, \alpha)$ is the rotor-stator magnetic voltage due to the armature field, and $\varepsilon_g(\gamma, \alpha)$ is a function representing the length of the flux tubes crossing the mechanical airgap.

The magnetic voltage can be determined by applying Ampere's law considering an elementary loop crossing the airgap two times [21], one of which is at the origin of the reference system $\gamma = 0$. Considering an anti-clockwise path as seen from the external side of the machine:

$$\mathscr{F}_{RS,2D}(\gamma, \bar{i}, \alpha) - \mathscr{F}_{RS,2D}(0, \bar{i}, \alpha) = \mathscr{M}_{2D}(\gamma, \bar{i}) \tag{8}$$

where $\mathscr{M}_{2D}(\gamma,\bar{i},\alpha)$ is the active sides' MMF:

$$\mathscr{M}_{2D}(\gamma,\bar{i}) = \bar{N}(\gamma)^T \cdot \bar{i} \tag{9}$$

where $\bar{N}(\gamma)$ is the vector of the winding functions (WFs) representative of the arrangement of the coils belonging to each phase. From (8), the rotor-stator magnetic tension can be seen as an equivalent MMF $\mathscr{F}_e(\gamma,\bar{i},\alpha)$ exciting the airgap defined as:

$$\mathscr{F}_e(\gamma,\bar{i},\alpha) = \mathscr{M}_{2D}(\gamma,\bar{i}) + \mathscr{F}_{RS,2D}(0,\bar{i},\alpha) \tag{10}$$

The second term $\mathscr{F}_{RS,2D}(0,\bar{i},\alpha)$ can be derived from the application of Gauss' law enforced for the generalized cylinder Ω_g as in Fig. 3, whose lateral surface is constituted by the average equipotential surface located at the airgap. Its application results in the following integral constraint:

$$\ell\int_0^1 B_{g,2D}(\gamma,\alpha,\bar{i})\cdot\tau_g(\gamma,\alpha)d\gamma = 0 \tag{11}$$

where $\tau_g(\gamma,\alpha)$ is a function that provides the profile of the medium magnetic-equipotential surface at the airgap. By substituting (7) in (11), it is possible to obtain the following equation:

$$\ell\int_0^1 \mu_0\frac{\tau_g(\gamma,\alpha)}{\varepsilon_g(\gamma,\alpha)}\cdot\mathscr{F}_{RS,2D}(\gamma,\bar{i},\alpha)d\gamma = 0 \tag{12}$$

and then, by substituting the expression of $\mathscr{F}_{RS,2D}$ given in (8), the Gauss' constraint becomes:

$$\ell\int_0^1 \mu_e(\gamma,\alpha)\cdot\left[\mathscr{F}_{RS,2D}(0,\bar{i},\alpha)+\mathscr{M}_{2D}(\gamma,\bar{i})\right]d\gamma = 0 \tag{13}$$

from which the unknown function $\mathscr{F}_{RS,2D}(0,\bar{i},\alpha)$ can be obtained as:

$$\begin{aligned}\mathscr{F}_{RS,2D}(0,\bar{i},\alpha) &= -\frac{\ell\int_0^1 \mu_e(\gamma,\alpha)\cdot[\mathscr{M}_{2D}(\gamma,\bar{i})]\,d\gamma}{\ell\int_0^1 \mu_e(\gamma,\alpha)d\gamma} = \\ &= -\int_0^1 \nu(\gamma,\alpha)\cdot\bar{N}(\gamma)^{\mathrm{T}}d\gamma\cdot\bar{i}\end{aligned} \tag{14}$$

where $\mu_e(\gamma,\alpha)$ and $\nu(\gamma,\alpha)$ are the equivalent permeability and the anisotropy functions defined respectively as:

$$\mu_e(\gamma,\alpha) = \mu_0\cdot\frac{\tau_g(\gamma,\alpha)}{\varepsilon_g(\gamma,\alpha)} \tag{15}$$

$$\nu(\gamma,\alpha) = \frac{\mu_e(\gamma,\alpha)}{\int_0^1 \mu_e(\gamma,\alpha)d\gamma} \tag{16}$$

Hence, the equivalent MMF defined in (10) can be rewritten as:

$$\mathscr{F}_e(\gamma,\bar{i},\alpha) = \left[\bar{N}(\gamma) - \int_0^1 \nu(\gamma,\alpha)\cdot\bar{N}(\gamma)d\gamma\right]^T\cdot\bar{i} \tag{17}$$

where the term in square brackets is defined as the equivalent WF $\bar{N}_e(\gamma,\alpha)$:

$$\bar{N}_e(\gamma,\alpha) = \bar{N}(\gamma) - \int_0^1 \nu(\gamma,\alpha)\cdot\bar{N}(\gamma)d\gamma \tag{18}$$

The equivalent MMF (17) coincides with the total MMF (9) minus its weighted mean value calculated over the whole tangential span assuming as weight the equivalent permeability function. In the isotropic scenario, the equivalent permeability function (15) is constant and the anisotropy function, from the definition given in (16), becomes $\nu(\gamma,\alpha)=1$. Hence, the equivalent MMF (17) is exactly equal to the total MMF minus its simple average.

Once the equivalent MMF is defined, the airgap flux density due to the armature field can be written in a compact form as a product of three terms:

$$B_{g,2D}(\gamma,\alpha,\bar{i}) = \frac{\mu_0}{\varepsilon_g(\gamma,\alpha)}\cdot\bar{N}_e(\gamma,\alpha)^T\cdot\bar{i} \tag{19}$$

providing the resolution of the magnetic problem related to the active sides' contribution when the geometry of the airgap, the winding arrangement, and the currents are known.

B. *Excitation field*

The excitation coil's magnetic contribution can be determined from Ampere's law applied to the axial loop Γ depicted in Fig. 4, i.e.:

$${}^1\mathscr{F}_{RS,0}(\gamma,\bar{i},\alpha) - {}^2\mathscr{F}_{RS,0}(\gamma,\bar{i},\alpha) = \mathscr{M}_0(\gamma,\bar{i},\alpha) \tag{20}$$

where ${}^k\mathscr{F}_{RS,0}(\gamma,\bar{i},\alpha)$ is the airgap magnetic tension due to the homopolar contributions of the k-section and $\mathscr{M}_0(\gamma,\bar{i},\alpha) = \mathscr{M}_0(\bar{i}) = N_{exc}i_{exc}$ is the MMF linked with the considered loop, which does not depend on the tangential coordinate γ. The relationship between the two can be found by enforcing Gauss' law on the cylinder Ξ_g encircling the whole rotor (depicted in orange in Fig. 4). Assuming null flux contribution at the end-caps, this results in:

$$\ell\int_0^1 [{}^1B_{g,0}(\gamma,\alpha,\bar{i}) + {}^2B_{g,0}(\gamma,\alpha,\bar{i})]\cdot\tau_g(\gamma,\alpha)d\gamma = 0 \tag{21}$$

This constraint enforces the overall homopolar flux of section 1 being equal, but with the opposite sign, to the one of section 2.

The airgap flux densities can be expressed as a function of the rotor-stator magnetic tensions, therefore:

$$\ell\int_0^1 \mu_e(\gamma,\alpha)\cdot[{}^1\mathscr{F}_{RS,0}(\gamma,\bar{i},\alpha) + {}^2\mathscr{F}_{RS,0}(\gamma,\bar{i},\alpha)]d\gamma = 0 \tag{22}$$

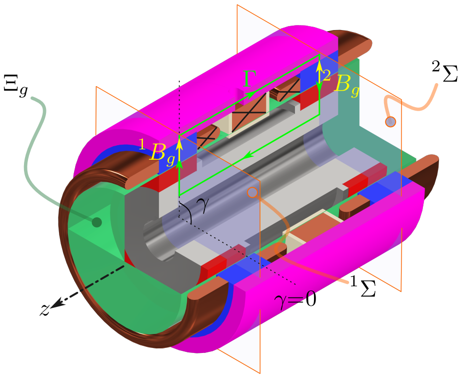

Fig. 4: Application of axial Ampere's and total Gauss' laws.

By substituting the relationship derived from the axial Ampere's law (20) in (22), one can obtain:

$$\ell \int_0^1 \mu_e(\gamma,\alpha)\cdot[2\cdot {}^2\mathscr{F}_{RS,0}(\gamma,\bar{i},\alpha)+\mathscr{M}_0(\bar{i})]d\gamma = 0 \tag{23}$$

from which is possible to derive the rotor-stator magnetic tension:

$${}^2\mathscr{F}_{RS,0}(\bar{i}) = -\int_0^1 \frac{\nu(\gamma,\alpha)}{2}\cdot\mathscr{M}_0(\bar{i})d\gamma \tag{24}$$

and considering that $\mathscr{M}_0$ does not depend on γ and $\int_0^1 \nu(\gamma,\alpha)d\gamma = 1$ [21], it follows that:

$${}^1\mathscr{F}_{RS,0}(\bar{i}) = -\,{}^2\mathscr{F}_{RS,0}(\bar{i}) = \frac{N_{exc}}{2}\cdot i_{exc} \tag{25}$$

As a consequence, the magnetic fields in the two sections due to the excitation coil contribution are:

$${}^1B_{g,exc}(\gamma,\alpha,\bar{i}) = -\,{}^2B_{g,exc}(\gamma,\alpha,\bar{i}) = \frac{\mu_0}{\varepsilon_g(\gamma,\alpha)}\cdot\frac{N_{exc}i_{exc}}{2} \tag{26}$$

As expected, the sign of the flux density is opposite in the two sections due to the enforcement of Gauss' law.

C. End-windings contribution

When split winding layouts are analysed, the end-windings located in the central part potentially contribute to the MMF when applying the axial Ampere's law as in (20). The crucial factor is the current linkage in the yz plane (see Fig. 5); as a consequence, if the leakage fluxes are neglected, the end-winding geometry (e.g. overhang length and shape) can be assumed to have a not significant impact on the principal flux distribution. Fig. 5 reports the assumed geometry of the end-windings for phases A, B, and C. Each arc can be seen as a portion of a solenoidal excitation coil and, according to the assumed conventions, the end-winding contribution to the axial MMF can be formally described through the WFs defined in (9).

Formally, the problem can be treated with the same approach adopted for the excitation coil in Section III-B. Therefore, the MMF in equation (20) can be described as a function of the EWs' winding functions:

$$\mathscr{M}_0(\gamma,\bar{i},\alpha) = \begin{bmatrix}{}^1\bar{N}(\gamma)^T & {}^2\bar{N}(\gamma)^T\end{bmatrix}\cdot\begin{bmatrix}\bar{i}_1\\ \bar{i}_2\end{bmatrix} \tag{27}$$

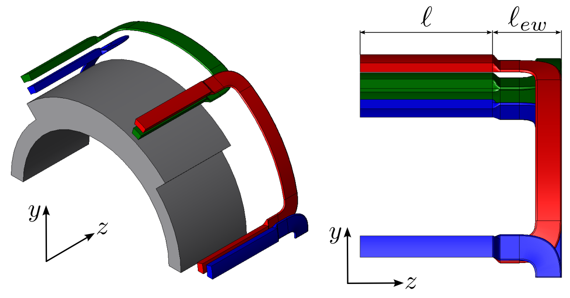

(a) (b)

Fig. 5: Assumed end-winding geometry for phases A, B, and C. Isometric view in (a) and yz view in (b).

Adopting the same approach used for the excitation coil field, the Gauss' law as in (21) can be enforced, and the equivalent magnetic tension can be calculated as in (24). The resulting ${}^1\mathscr{F}_{e,EW}(\alpha,\bar{i})$ and ${}^2\mathscr{F}_{e,EW}(\alpha,\bar{i})$ are the equivalent end-windings MMF applied between the rotor and stator:

$${}^1\mathscr{F}_{e,EW}(\alpha,\bar{i}) = {}^1\bar{N}_{e,EW}(\alpha)^T\cdot\bar{i}_1 + {}^2\bar{N}_{e,EW}(\alpha)^T\cdot\bar{i}_2 \tag{28a}$$

$${}^2\mathscr{F}_{e,EW}(\alpha,\bar{i}) = -\,{}^1\bar{N}_{e,EW}(\alpha)^T\cdot\bar{i}_1 - {}^2\bar{N}_{e,EW}\alpha)^T\cdot\bar{i}_2 \tag{28b}$$

where the equivalent end-WFs are calculated as:

$${}^1\bar{N}_{e,EW}(\alpha) = \int_0^1 \frac{\nu(\gamma,\alpha)}{2}\cdot{}^1\bar{N}(\gamma)d\gamma \tag{29a}$$

$${}^2\bar{N}_{e,EW}(\alpha) = \int_0^1 \frac{\nu(\gamma,\alpha)}{2}\cdot{}^2\bar{N}(\gamma)d\gamma \tag{29b}$$

IV. FLUX LINKAGES AND INDUCTANCES

The total magnetic field can be written as the sum of three contributions: the armature field, the excitation coil field, and the end-windings field as in (5)-(6). Equations (30)-(31) report the expression of the total magnetic field at the airgap combining the final expressions derived in the previous sections. The term in square brackets can be seen as a total equivalent MMF exciting the airgap $\mathscr{F}_{E,tot}(\gamma,\alpha,\bar{i})$.

The full inductance matrix $\mathbf{L}(\alpha)$ can be written in the following form:

$$\mathbf{L}(\alpha) = \begin{bmatrix} {}^{\mathbf{1,1}}\mathbf{L}(\alpha) & {}^{\mathbf{1,2}}\mathbf{L}(\alpha) & \bar{L}_{1,exc}(\alpha)\\ {}^{\mathbf{1,2}}\mathbf{L}(\alpha)^T & {}^{\mathbf{2,2}}\mathbf{L}(\alpha) & \bar{L}_{2,exc}(\alpha)\\ \bar{L}_{1,exc}(\alpha)^T & \bar{L}_{2,exc}(\alpha)^T & L_{exc}(\alpha)\end{bmatrix} \tag{36}$$

where ${}^{\mathbf{k,k}}\mathbf{L}$ is the sub-matrix of inductances of the k-section, ${}^{\mathbf{k,h}}\mathbf{L}$ is the sub-matrix of the mutual inductances between the k- and h-section, $\bar{L}_{k,exc}$ is the vector of the mutual inductances between the excitation coil and the k-section, while L_{exc} is the excitation coil self-inductance. Equation (37) permits the evaluation of the linkage flux function ${}^k\bar{\Psi}(\alpha,\bar{i})$, where the integration is computed at the medium magnetic-equipotential surface.

$${}^k\bar{\Psi}(\alpha,\bar{i}) = \ell\int_0^1 {}^kB_g(\gamma,\alpha,\bar{i})\cdot\tau_g(\gamma,\alpha)\cdot{}^k\bar{N}(\gamma)d\gamma \tag{37}$$

By substituting the expression of the airgap flux density and keeping in mind the definition of the equivalent permeability (15), the various sub-matrices defined in (36) are derived as in equations (32)-(35). Using the superposition principle, the sub-matrix of inductances (32)-(33) can be decomposed into two distinct contributions:

1) $\mathbf{L_{2D}}$, which is purely related to the active sides MMF contribution, equal to the classical 2D resolution of the problem;
2) $\mathbf{L_{EW}}$, which is the contribution related to the end-windings MMF related to the specific section.

It is worth highlighting that the sub-matrix ${}^{\mathbf{1,2}}\mathbf{L}(\alpha)$ in (34), which is responsible for the mutual coupling between the two sections, depends only on the end-windings MMF. In the case of pass-through armature layouts (Fig. 1) the axial mutual coupling is zero, being ${}^1\bar{N}_{e,EW} = {}^2\bar{N}_{e,EW} = 0$. Indeed, for

$$ {}^{1}B_g(\gamma,\alpha,\bar{i}) = \frac{\mu_0}{\varepsilon_g(\gamma,\alpha)} \cdot \left[\frac{N_{exc} i_{exc}}{2} + \int_0^1 \frac{\nu(\gamma,\alpha)}{2}\, {}^{1}\bar{N}(\gamma)^T d\gamma \cdot \bar{i}_1 + \int_0^1 \frac{\nu(\gamma,\alpha)}{2}\, {}^{2}\bar{N}(\gamma)^T d\gamma \cdot \bar{i}_2 + {}^{1}\bar{N}_e(\gamma,\alpha)^T \cdot \bar{i}_1 \right] \tag{30} $$

$$ {}^{2}B_g(\gamma,\alpha,\bar{i}) = -\frac{\mu_0}{\varepsilon_g(\gamma,\alpha)} \cdot \left[\frac{N_{exc} i_{exc}}{2} + \int_0^1 \frac{\nu(\gamma,\alpha)}{2}\, {}^{1}\bar{N}(\gamma)^T d\gamma \cdot \bar{i}_1 + \int_0^1 \frac{\nu(\gamma,\alpha)}{2}\, {}^{2}\bar{N}(\gamma)^T d\gamma \cdot \bar{i}_2 + {}^{2}\bar{N}_e(\gamma,\alpha)^T \cdot \bar{i}_2 \right] \tag{31} $$

$$ {}^{\mathbf{1,1}}\mathbf{L}(\alpha) = \ell \int_0^1 \mu_e(\gamma,\alpha) \cdot \left[{}^{1}\bar{N}_e(\gamma,\alpha)^T + {}^{1}\bar{N}_{e,EW}(\alpha)^T \right] \cdot {}^{1}\bar{N}(\gamma) d\gamma = {}^{\mathbf{1,1}}\mathbf{L}_{\mathbf{2D}}(\alpha) + {}^{\mathbf{1,1}}\mathbf{L}_{\mathbf{EW}}(\alpha) \tag{32} $$

$$ {}^{\mathbf{2,2}}\mathbf{L}(\alpha) = \ell \int_0^1 \mu_e(\gamma,\alpha) \cdot \left[{}^{2}\bar{N}_e(\gamma,\alpha)^T + {}^{2}\bar{N}_{e,EW}(\alpha)^T \right] \cdot {}^{2}\bar{N}(\gamma) d\gamma = {}^{\mathbf{2,2}}\mathbf{L}_{\mathbf{2D}}(\alpha) + {}^{\mathbf{2,2}}\mathbf{L}_{\mathbf{EW}}(\alpha) \tag{33} $$

$$ {}^{\mathbf{1,2}}\mathbf{L}(\alpha) = \ell \int_0^1 \mu_e(\gamma,\alpha) \cdot {}^{2}\bar{N}_{e,EW}(\alpha)^T \cdot {}^{1}\bar{N}(\gamma) d\gamma \tag{34} $$

$$ \bar{L}_{1,exc}(\alpha) = \ell \int_0^1 \mu_e(\gamma,\alpha) \cdot \frac{N_{exc}}{2} \cdot {}^{1}\bar{N}(\gamma) d\gamma \qquad \bar{L}_{2,exc}(\alpha) = -\ell \int_0^1 \mu_e(\gamma,\alpha) \cdot \frac{N_{exc}}{2} \cdot {}^{2}\bar{N}(\gamma) d\gamma \tag{35} $$

---

the pass-through configuration, the EW contribution is zero due to the absence of any end-winding part located between the two machine sections going in the circumferential direction (the end-winding connection is only axial in this case as shown in Fig. 1). The excitation coil self-inductance can be computed from the homopolar flux ϕ_0 when only the excitation coil is supplied (i.e., $\bar{i}_1 = \bar{i}_2 = \bar{0}$). In this scenario, the linkage flux can be calculated from the homopolar flux re-closing through the rotor sleeve:

$$ \phi_0(\alpha, i_{exc}) = \ell \int_0^1 {}^{1}B_g(\gamma,\alpha,\bar{i}) \cdot \tau_g(\gamma,\alpha) d\gamma \Big|_{(\bar{i}_1=\bar{i}_2=\bar{0})} \tag{38} $$

and by substituting equations (15) and (26), the excitation coil self-inductance $L_{exc}(\alpha)$ can be computed as:

$$ L_{exc}(\alpha) = \frac{N_{exc}\phi_0(\alpha, i_{exc})}{i_{exc}} = \frac{N_{exc}^2}{2} \ell \int_0^1 \mu_e(\gamma,\alpha) d\gamma \tag{39} $$

V. NUMERICAL IMPLEMENTATION OF THE MODEL

The model proposed in the previous section has been numerically implemented in the Matlab-Simulink environment. The design presented in [25], whose main parameters are reported in Table I, is considered as a case study to validate the proposed analytical modelling approach.

The SHM is designed to be a generation unit intended to supply two independent DC links via diode rectifiers. In particular, each machine section supplies two series connected 3-phase diode rectifiers as in the classic 12-pulses arrangements. The selected winding layout, which features 2 three-phase sets shifted by $\pi/6$ electrical degrees [26], is made of 12 coils per machine section, arranged in a double-layer layout as depicted in Fig. 6. Each phase is then composed of 2 coils connected in anti-series (A-a, B-b, C-c and U-u, V-v, W-w, respectively) shown in the phasor diagram with arrows having the same colour.

TABLE I: Case study specifications

Symbol	Parameter	Unit	Value
P_n	Rated Power	kW	1.2
Ω_n	Rated Speed	rpm	6000
$V_{DC,n}$	Rated DC-link Voltage	V	320
$i_{exc,n}$	Rated Excitation Current	A	120
p	Pairs of Poles	-	2
Q	Number of Slots	-	24
n_{ph}	Number of Phases	-	$24+1$

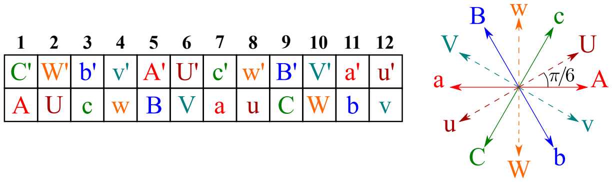

1	2	3	4	5	6	7	8	9	10	11	12
C'	W'	b'	v'	A'	U'	c'	w'	B'	V'	a'	u'
A	U	c	w	B	V	a	u	C	W	b	v

Fig. 6: Winding layout under 1 pole pair.

A. Airgap profile definition

The impact of the slot opening on the flux distribution is incorporated in the function $\varepsilon_g(\gamma,\alpha)$, which describes the radial length of the flux tubes crossing the mechanical airgap (when the airgap flux lines are mainly radial). The function $\varepsilon_g(\gamma,\alpha)$ can be seen as the difference between the stator and rotor equipotential lines as in (40).

$$ \varepsilon_g(\gamma,\alpha) = r_s(\gamma) - r_r(\gamma,\alpha) \tag{40} $$

The methodology presented in [27] is hereafter adopted for modelling the equivalent airgap length at the slot openings (r_s) which uses an infinitely deep slot assumption. Regarding the function describing the rotor magnetic-equipotential (r_r), a trapezoidal pattern describes with good accuracy the rotor saliency for the geometry under analysis. The implemented stator, rotor, and medium (r_g) magnetic-equipotential line at the airgap are reported in Fig. 7. Considering the small anisotropy introduced by the slot openings and airgap radius far greater than the slot openings depths, a cylindrical magnetic equipotential surface can be assumed, resulting in the expression of $\tau_g(\gamma,\alpha)$ given in (41).

$$ \tau_g(\gamma,\alpha) = 2\pi \cdot \frac{r_s(\gamma) + r_r(\gamma,\alpha)}{2} = 2\pi r_g(\gamma,\alpha) \tag{41} $$

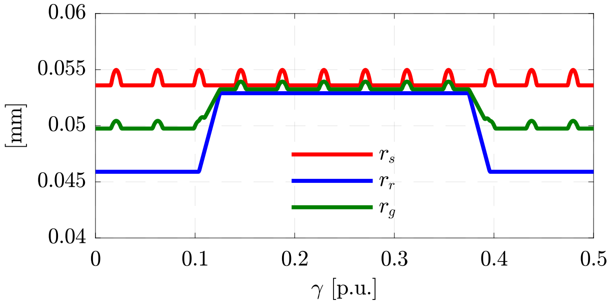

Fig. 7: Airgap profiles modelling.

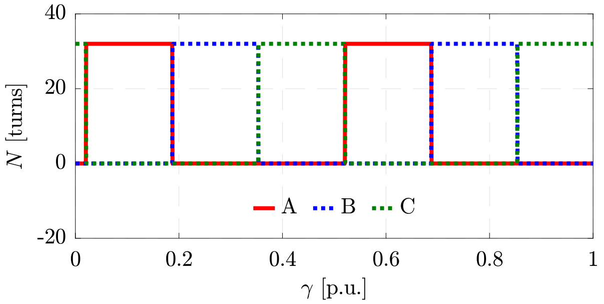

Fig. 8: WF implementation for the armature winding and end-windings.

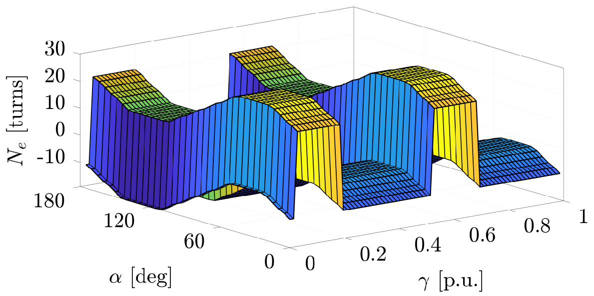

Fig. 9: Equivalent WF for the active sides of phase A.

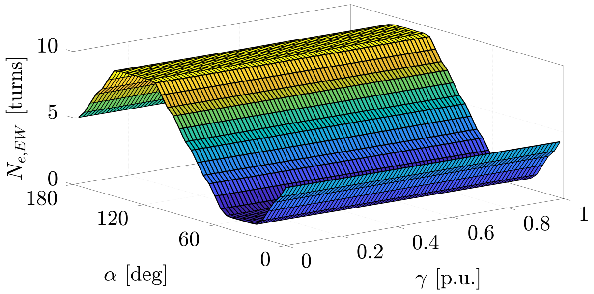

Fig. 10: Equivalent WF for the end-windings of phase A.

B. Winding functions

An accurate implementation of the WFs allows the effective representation of the spatial multi-harmonic nature of the MMFs. The MMF contribution of the active sides located in one slot may be concentrated at the slot opening [22] and this results in the classical square-wave WFs as depicted in Fig. 8. The same implementation can be used to describe the end-windings WFs. Nevertheless, the active sides' and EWs' WFs differ when their equivalent effect is considered. Indeed, following the integrations defined in equations (18) and (29), the equivalent phase A WF for the active sides $\bar{N}_e$ and EWs $\bar{N}_{e,EW}$ feature the trend shown in Fig. 9 and 10, respectively. Unlike $\bar{N}_e$, the $\bar{N}_{e,EW}$ function is constant along γ, i.e. the resulting MMF at the airgap does not depend on the angular position. However, its amplitude does depend on the rotor position α.

VI. FE MODEL VALIDATION

A 3D FE model, depicted in Fig. 11, is built in the JMAG-Designer environment with the aim of validating the proposed analytical model. Linear magnetic materials are assigned to the iron cores and multi-static current-fed simulations are carried out capturing the airgap flux density, the inductances and induced voltage as a function of the rotor position α in the no-load and load operative conditions. These operating points have been selected because the SHM considered has been designed as a generator unit mainly working at the rated condition. In the following subsections, a detailed comparison between FE and analytical performance is presented highlighting the benefits and limitations of the proposed approach.

A. Airgap flux density

The FE airgap flux densities are extracted at the average airgap line located at the mid-plane per each machine section. Fig. 12 reports the analytical and FE no-load flux density for both axial sections when the excitation level is $i_{exc} = 120\,\text{A}$. An outstanding match is clearly visible with both rotor saliency and slot opening effects well captured. Indeed, the relative error on the maximum airgap flux density is 2.4%. As expected, the airgap flux density features opposite signs in the two sections.

Fig. 13 shows the airgap magnetic field distribution in the two sections for one specific rotor position when only one section is supplied with the rated current while both excitation and the other section coils are disabled, i.e. $\bar{i}_1 = \bar{i}_n$ and $\bar{i}_2 = i_{exc} = 0$. This unbalanced supply condition permits highlighting the mutual coupling between the two sections. Indeed, despite there is not any excitation source in section 2 (i.e., $\bar{i}_2 = 0$) and null excitation current $i_{exc} = 0$, there

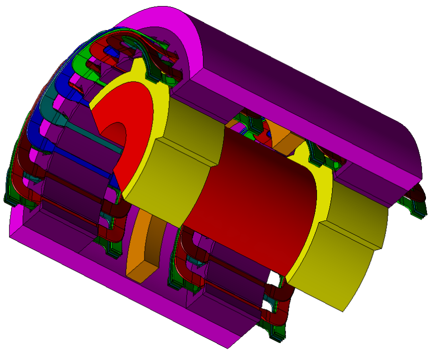

Fig. 11: 3D FE model built in JMAG-Designer.

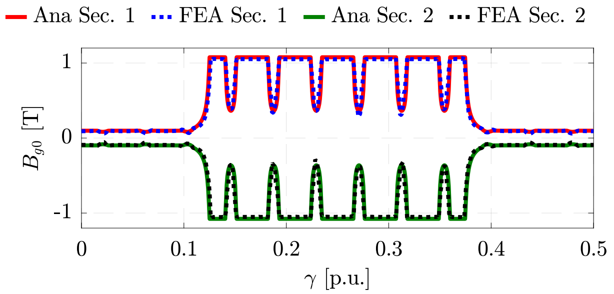

Fig. 12: No-Load airgap flux-density in sections 1 and 2 for a given rotor position: analytical vs. FEA.

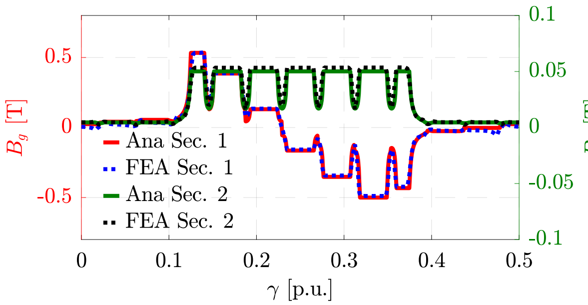

Fig. 13: Airgap flux-density distribution when only section one is supplied with the rated current. The analytical and FEA distributions in sections 1 (left y-axis) and 2 (right y-axis) for a given rotor position are reported.

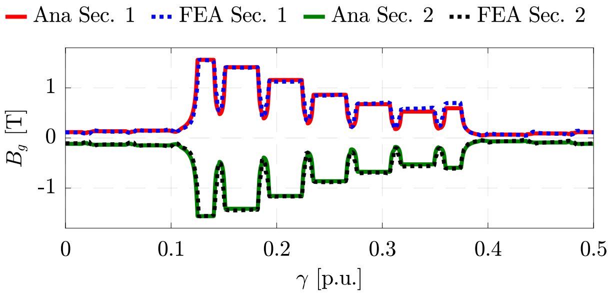

Fig. 14: Airgap flux-density distribution at the rated operative point: analytical vs. FEA.

is a non-negligible flux density at the airgap rising from the equivalent end-winding MMF (second term in the square bracket of (31)):

$$^{2}B_g(\gamma,\alpha,\bar{i}) = -\frac{\mu_0}{\varepsilon_g(\gamma,\alpha)} \cdot \int_0^1 \frac{\nu(\gamma,\alpha)}{2} \cdot {}^{1}\bar{N}(\gamma)^T d\gamma \cdot \bar{i}_1 \quad (42)$$

The integration leads to an equivalent MMF that does not depend on the tangential position γ. Nevertheless, its amplitude features a dependence on the rotor angular position α.

In Fig. 14, the total airgap flux density at the rated operative point is reported. Both sections, as well as the excitation coil, are supplied. Hence, the resulting field distribution is the sum of all the contributions reported in equations (30)-(31). In all the reported three cases, the match between FE and analytical prediction is practically perfect. Indeed, the relative error on the amplitude of the fundamental component at no-load and load is 1.5% and 0.9%, respectively.

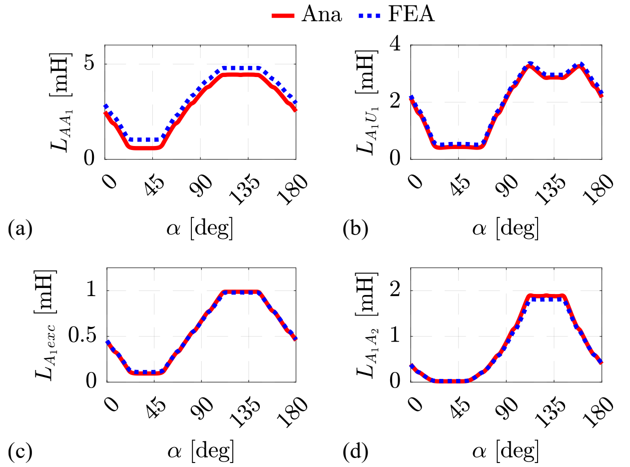

(a) (b) (c) (d)

Fig. 15: Inductances as a function of the rotor position: a) phase A self-inductance, b) mutual inductance between phase A and U, c) mutual inductance between phase A and the excitation coil, and d) mutual inductance between the two phases A.

B. Inductances and voltages

Fig. 15 reports the most important inductances as a function of the rotor position α computed analytically and by FEA. The self-inductance of phase A section 1 (Fig. 15 (a)) is analytically well captured with an error in the first harmonic prediction around 1.5%. Its variation with the rotor position is due to the anisotropic nature of the machine. The mismatch is independent from the rotor position, i.e. it is mainly an offset (0.4 mH, 12% of the average) therefore may be attributed to the leakage fluxes which do not depend on the rotor position and are not kept into account in the analytical modelling. Fig. 15 (b) reports the results of the mutual inductance between two phases (A and U) of the same section not sharing the same slots (the winding layout is double layer) therefore the leakage does not affect its value. In this case, the analytical model perfectly captures the mutual inductance trend. The same applies to the mutual inductance between the excitation coil and phase A which is also well predicted as depicted in Fig. 15 (c). The last subfigure Fig. 15 (d) is related to the mutual inductance between two phases belonging to different axial sections. Also in this case, the match is practically perfect. The resulting relative relative errors on the amplitude of the fundamental components are 0.1%, 2.9%, and 5%, respectively.

With the aim of analysing the different contributions to the inductances due to armature MMF and end-winding MMF (see (32)), Fig. 16 and Fig. 17 report the breakdown of the different components of L_{A1A1} and L_{A1u1}. Analysing these two figures yields the conclusion that neglecting the end winding MMF contribution leads to a relevant performance estimation error in linear operating conditions. Indeed, the inductance calculated considering only the MMF of the active sides is different than the one predicted by FEA. As a direct consequence of the

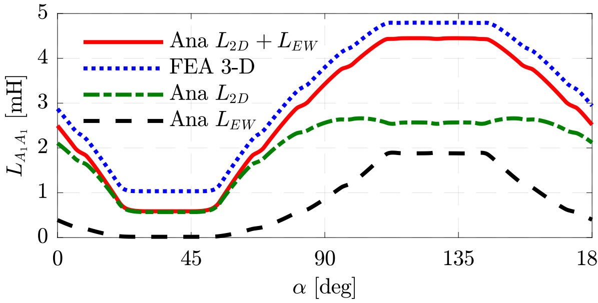

Fig. 16: Breakdown of different components for the self-inductance of phase A.

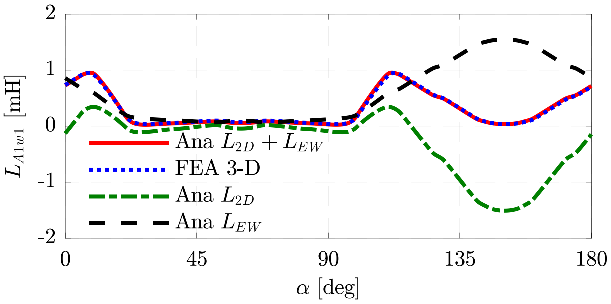

Fig. 17: Breakdown of different components for the mutual inductance between phase A and u belonging to the same section.

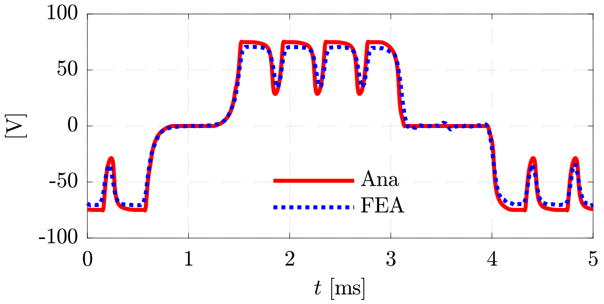

Fig. 18: Phase A back-EMF at the rated operative condition ($i_{exc} = 120\,\mathrm{A}$): analytical vs. FEA.

good inductance prediction, also the induced voltage waveform prediction well matches the FE one. Fig. 18 shows the back-EMF at the rated speed and rated excitation current, resulting in a relative error of 3.2% on the amplitude of the fundamental component.

C. Discussion

Table II reports the comparison between the computational time required to solve the analytical-numerical model and the 3D FE model for calculating the inductances. An electrical period is simulated and the number of discretisation points of the rotor position α is reported. The same computer featuring 256 GB of RAM and an AMD Ryzen Threadripper PRO 5955WX 16-Cores @ 4 GHz has been used to perform both computations. The advantage in terms of computational burden is crystal clear.

TABLE II: Performance comparison.

	Number of Points	Computational Time
Analytical-Numerical	720	6s
3D FEA	200	11h 13min 46s

VII. EXPERIMENTAL VALIDATION

The homopolar generator featuring the specifications reported in Table I has been manufactured and assembled. The stator and rotor sleeves are made of solid magnetic mild steel EN1A, while the rotor poles and the stator stacks are laminated in M235-35A and NO20, respectively. The direct oil-cooled excitation coil is manufactured with a hollow copper pipe, where a high-temperature fibreglass sleeve featuring a silicone rubber coating provides the turn-to-turn electrical insulation [25]. It consists of 10 turns, geometrically deployed on 2 radial layers. The outer and inner diameters are $4\,\mathrm{mm}$ and $2.8\,\mathrm{mm}$, respectively. The different parts are reported in Fig. 19.

The experimental platform used to validate the proposed analytical model presented is shown in Fig. 20. It consists of a $14.1\,\mathrm{kW}$ Induction Machine (IM), acting as a prime mover, mounted on the same shaft of the SHM. Closed-loop speed and position controls are performed via a Control Techniques (CT) M700 industrial drive. The excitation coil is direct oil-cooled via a TT-188 temperature control unit, which provides the active control of the inlet coolant temperature. The BP Turbo Oil 2389 is selected as a coolant thanks to its low kinematic viscosity value and good thermal properties. The coolant flow rate is regulated through a needle valve. The rated flow rate and inlet oil temperature $0.83\,\mathrm{l/min}$ and $70\,°\mathrm{C}$ respectively, corresponding to an inlet-outlet coolant temperature difference of $8\,°\mathrm{C}$ and average copper temperature of $77.4\,°\mathrm{C}$.

An open end-winding configuration of the armature windings of the machine under test permits access to the different coil terminals. Two different series of tests have been performed: the back-EMFs tests at different excitation levels and the inductance measurements vs. rotor position α.

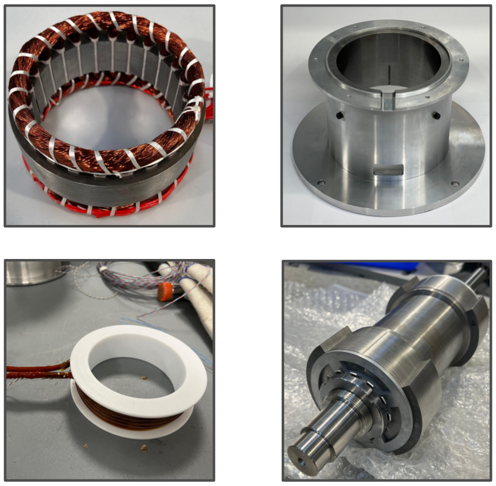
Stator and Winding
Housing and Sleeve
Excitation Coil
Full Rotor

Fig. 19: Prototype parts.

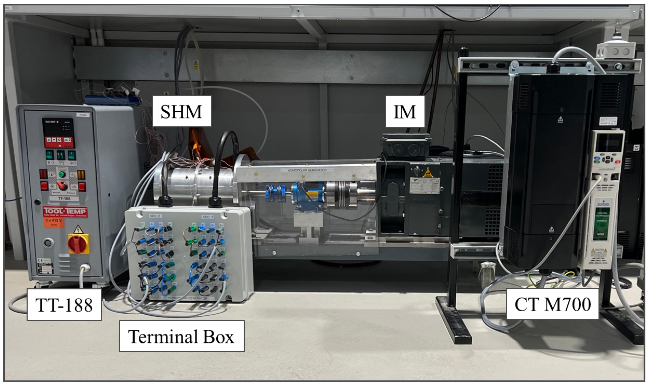

Fig. 20: Experimental rig layout.

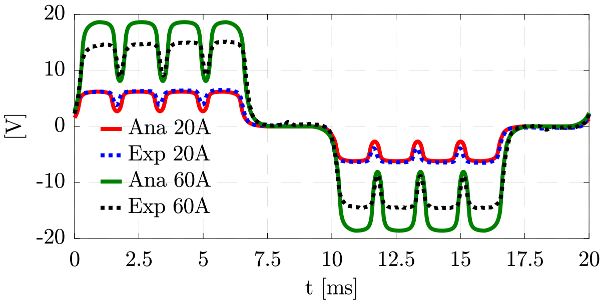

(a) *Phase A-a at* $i_{exc} = 20\,\mathrm{A}$ *and* $i_{exc} = 60\,\mathrm{A}$.

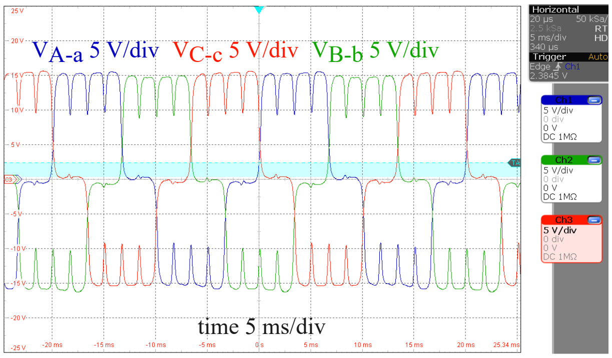

(b) *Acquisition at* $i_{exc} = 60\,\mathrm{A}$ *for phases A-a, B-b, and C-c.*

Fig. 21: Back-EMFs at 1500 rpm: analytical vs. experimental results.

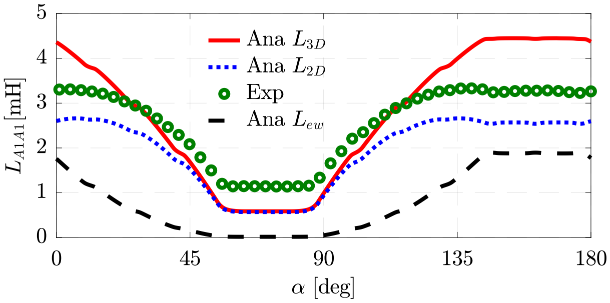

Fig. 22: Phase A self-inductance: analytical vs. experimental results.

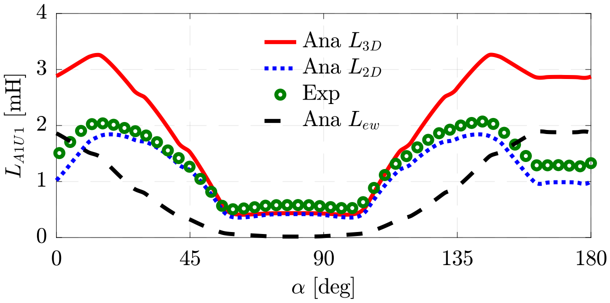

Fig. 23: Mutual inductance between phase A and U belonging to the same section: analytical vs. experimental results.

During the first test, the coil terminals were left open, the desired rotational speed was imposed by the prime mover while the excitation coil was supplied via a DC power supply. The phase A-a back-EMF at 1500 rpm and $i_{exc} = 20\,\mathrm{A}$ analytically estimated is compared with the measured one, as shown in Fig. 21a. The good match demonstrates that the analytical model is capable of accurately predicting the no-load performance (relative error on the fundamental component 9.6%). Nevertheless, when the same test was performed at a higher excitation current ($i_{exc} = 60\,\mathrm{A}$), a mismatch becomes visible, with the relative error increasing to 18%. This can be surely ascribed to the stator and rotor sleeves' saturation. In fact, the mild steel adopted for both stator and rotor sleeves behaves quite differently than an ideal material where the MMF drops in the iron core can be neglected. A screenshot of the oscilloscope capturing the back-EMF acquisition of phases A-a, B-b, and C-c is reported (Fig. 21b).

The second series of tests aimed at measuring the inductance behaviour as a function of the rotor position α was carried out by supplying a single coil belonging to the phase k with a controllable AC current supply (Chroma Programmable AC Source 61511). For a given angular position α, the amplitude of the induced voltage phasors and current phasor ($|\dot{V}_h|$, for $h = 1, \ldots, n_{ph}$ and $|\dot{I}_k|$) were measured with a Rohde & Schwarz RTE 1024 oscilloscope. The k-phase self inductance (L_{kk}) and the mutual inductance between the k- and h-phase (M_{kh}) were respectively calculated as:

$$L_{kk} = \frac{\sqrt{|Z_k|^2 - R_k^2}}{\omega} \qquad M_{kh} = \frac{|\dot{V}_k|}{|\dot{I}_h| \cdot \omega} \tag{43}$$

where ω is the supply angular frequency, $|Z_k| = |\dot{V}_k|/|\dot{I}_k|$ and R_k are the k-phase impedance magnitude and resistance. The latter was measured through a QuadTech 1730 LCR meter at the same supply angular frequency. The test was performed with a current of 1 Arms, which is below the rated value of the machine. The rotor position was controlled by the prime mover industrial drive implementing a closed-loop position control. The measurement was carried out for 100 equally spaced angular positions under the electrical period.

The phase A self-inductance measurement is reported in Fig. 22 along with the analytical prediction of its various constituent components. The experimental measurement lies between the 2D and 3D analytical results, i.e. the one predicted considering the MMF contribution of the active side and the overall winding path, respectively. This behaviour can be attributed to two factors: the sleeves' magnetic saturation and the leakage. Indeed, both these factors are not considered in the analytical model. Fig. 23 reports the mutual inductance between phases belonging to the same section not sharing any slot. In this last case too, the measurement stays between the 2D and 3D analytical results but the mismatch can only be ascribed to the sleeves' saturation as the leakage inductance is zero. In the real non-linear scenario, the end-winding share of the inductance is smaller due to the lower magnetic permeability featured by the mild steel.

VIII. CONCLUSIONS

An analytical-numerical model of the governing electromagnetic equations of synchronous homopolar machines is proposed. The outlined general approach allows for the analysis of both split and passing winding configurations. It can account for the MMF harmonics, the slotting effect, and the end-windings' MMF contribution to the axial flux. The results demonstrate that the proposed analytical model is able of effectively compute, for different operative conditions, the airgap flux density, the linkage fluxes, and ultimately the matrix of the inductances as a function of the rotor position. The model predictions have been fully validated through several 3D FEAs and a comprehensive experimental test campaign carried out on a $1.2\,\mathrm{kW}$ laboratory scale prototype. The results show the importance of considering all the MMF sources in the computation of the airgap flux densities including the one due to the end-winding parts. The effect of this definitely unusual MMF source is weakened when considering the magnetic non-linear scenario. Given the complex machine operating principle and its peculiar 3D main flux path requiring a computationally expensive FEA for the performance prediction, the proposed analytical model - despite its limitations - could potentially serve as a fundamental basis for expeditious design optimization of this machine topology.

ACKNOWLEDGEMENTS

The authors would like to thank POWERSYS for providing JMAG software, as FEA packages for electric machine design, and for their support in carrying out this study.

The authors would like to express their sincere appreciation to the PEMC technicians for their crucial support in this work.

REFERENCES

[1] E. A. Erdelyi, F. S. V. Ahamed, and R. E. Hopkins, "Design considerations and optimization of homopolar inductor alternators of aerospace power systems," *IEEE Transactions on Aerospace and Electronic Systems*, vol. AES-2, no. 4, pp. 106–115, 1966.

[2] C. Ye, J. Yang, F. Xiong, and Z. Q. Zhu, "Relationship between homopolar inductor machine and wound-field synchronous machine," *IEEE Transactions on Industrial Electronics*, vol. 67, no. 2, pp. 919–930, 2020.

[3] A. Vannini, A. Marfoli, L. Papini, P. Bolognesi, and C. Gerada, "Materials for electric machines suited for high-temperature applications: a survey," in *2021 IEEE Workshop on Electrical Machines Design, Control and Diagnosis (WEMDCD)*, 2021, pp. 101–106.

[4] M. Murataliyev, M. Degano, M. Di Nardo, N. Bianchi, and C. Gerada, "Synchronous reluctance machines: A comprehensive review and technology comparison," *Proceedings of the IEEE*, vol. 110, no. 3, pp. 382–399, 2022.

[5] E. Severson, R. Nilssen, T. Undeland, and N. Mohan, "Magnetic equivalent circuit modeling of the ac homopolar machine for flywheel energy storage," *IEEE Transactions on Energy Conversion*, vol. 30, no. 4, pp. 1670–1678, 2015.

[6] K. Sivasubramaniam, E. T. Laskaris, M. R. Shah, J. W. Bray, and N. R. Garrigan, "High-temperature superconducting homopolar inductor alternator for marine applications," *IEEE Transactions on Applied Superconductivity*, vol. 18, no. 1, pp. 1–6, 2008.

[7] M. Lashkevich, A. Anuchin, D. Aliamkin, and F. Briz, "Investigation of self-sensing rotor position estimation methods for synchronous homopolar motor in traction applications," in *IECON 2017 - 43rd Annual Conference of the IEEE Industrial Electronics Society*, 2017, pp. 8225–8229.

[8] V. Dmitrievskii, V. Kazakbaev, and V. Prakht, "Performance comparison of traction synchronous motors with ferrite magnets for a subway train: Reluctance versus homopolar variants," *Applied Sciences*, vol. 13, no. 17, 2023. [Online]. Available: https://www.mdpi.com/2076-3417/13/17/9988

[9] H. Devred, M. Martinez, and J. Huonic, "150 kVA, 56000 rpm, turbo engine integrated homopolar electrical generator," in *IEEE International Electric Machines and Drives Conference. IEMDC'99. Proceedings (Cat. No.99EX272)*, 1999, pp. 749–751.

[10] J. Ma, Y. Pan, X. Luo, H. Xiao, J. Yang, N. Simpson, and P. Mellor, "Design of a 10 kw superconducting homopolar inductor machine based on hts rebco magnet," *IEEE Transactions on Applied Superconductivity*, vol. 34, no. 5, pp. 1–7, 2024.

[11] E. Severson, R. Nilssen, T. Undeland, and N. Mohan, "Outer-rotor ac homopolar motors for flywheel energy storage," in *7th IET International Conference on Power Electronics, Machines and Drives (PEMD 2014)*, 2014, pp. 1–6.

[12] J. Yang, P. Liu, C. Ye, L. Wang, X. Zhang, and S. Huang, "Multidisciplinary design of high-speed solid rotor homopolar inductor machine for flywheel energy storage system," *IEEE Transactions on Transportation Electrification*, vol. 7, no. 2, pp. 485–496, 2021.

[13] A. Vannini, I. Kougioulis, M. Murataliyev, A. L. Rocca, A. Marfoli, and C. Gerada, "An improved homopolar generator topology for reduced dc-link voltage ripple using passive diode rectifiers," in *2023 IEEE Workshop on Power Electronics for Aerospace Applications (PEASA)*, 2023, pp. 1–6.

[14] J. Asama, D. Suzuki, T. Oiwa, and A. Chiba, "Development of a homopolar bearingless motor with concentrated winding for high speed applications," in *2018 International Power Electronics Conference (IPEC-Niigata 2018 -ECCE Asia)*, 2018, pp. 157–160.

[15] W. Li, K. T. Chau, T. W. Ching, Y. Wang, and M. Chen, "Design of a high-speed superconducting bearingless machine for flywheel energy storage systems," *IEEE Transactions on Applied Superconductivity*, vol. 25, no. 3, pp. 1–4, 2015.

[16] R. Köster and A. Binder, "Electromagnetic design considerations on hts excited homopolar inductor alternators," in *2022 International Symposium on Power Electronics, Electrical Drives, Automation and Motion (SPEEDAM)*, 2022, pp. 479–484.

[17] V. Dmitrievskii, V. Prakht, A. Anuchin, and V. Kazakbaev, "Traction synchronous homopolar motor: Simplified computation technique and experimental validation," *IEEE Access*, vol. 8, pp. 185 112–185 120, 2020.

[18] E. Severson, R. Nilssen, T. Undeland, and N. Mohan, "Analysis of the bearingless ac homopolar motor," in *2012 XXth International Conference on Electrical Machines*, 2012, pp. 570–576.

[19] J. Yang, Q. Li, C. Guo, Y. Tu, S. Huang, and C. Ye, "Comparative study of homopolar inductor machines with different rotor structures for flywheel energy storage system," in *2021 IEEE 4th International Electrical and Energy Conference (CIEEC)*, 2021, pp. 1–6.

[20] J. Yang, C. Ye, S. Huang, Y. Li, F. Xiong, Y. Zhou, and W. Xu, "Analysis of the electromagnetic performance of homopolar inductor machine through nonlinear magnetic equivalent circuit and air-gap permeance function," *IEEE Transactions on Industry Applications*, vol. 56, no. 1, pp. 267–276, 2020.

[21] P. Bolognesi, "A mid-complexity analysis of long-drum-type electric machines suitable for circuital modeling," in *2008 18th International Conference on Electrical Machines*, 2008, pp. 1–5.

[22] A. Marfoli, L. Papini, P. Bolognesi, and C. Gerada, "An analytical-numerical approach to model and analyse squirrel cage induction motors," *IEEE Transactions on Energy Conversion*, vol. 36, no. 1, pp. 421–430, 2021.

[23] S. Nuzzo, P. Bolognesi, C. Gerada, and M. Galea, "Simplified damper cage circuital model and fast analytical–numerical approach for the

analysis of synchronous generators," *IEEE Transactions on Industrial Electronics*, vol. 66, no. 11, pp. 8361–8371, 2019.

[24] A. Vannini, C. Simonelli, A. Marfoli, L. Papini, P. Bolognesi, and C. Gerada, "Modelling, analysis, and design of a line-start permanent magnet synchronous motor," in *2022 International Conference on Electrical Machines (ICEM)*, 2022, pp. 834–840.

[25] A. Vannini, A. L. Rocca, M. Cooper, A. Marfoli, L. Papini, P. Bolognesi, and C. Gerada, "Design of a dual dc-bus homopolar generator implementing a direct-cooled excitation coil," in *2023 IEEE International Electric Machines & Drives Conference (IEMDC)*, 2023, pp. 1–7.

[26] G. Sulligoi, A. Tessarolo, V. Benucci, M. Baret, A. Rebora, and A. Taffone, "Modeling, simulation and experimental validation of a generation system for medium-voltage dc integrated power systems," in *2009 IEEE Electric Ship Technologies Symposium*, 2009, pp. 129–134.

[27] B. Gaussens, E. Hoang, O. de la Barriere, J. Saint-Michel, M. Lecrivain, and M. Gabsi, "Analytical approach for air-gap modeling of field-excited flux-switching machine: No-load operation," *IEEE Transactions on Magnetics*, vol. 48, no. 9, pp. 2505–2517, 2012.

Amedeo Vannini received his M.Sc. degree (cum laude) in Electrical Engineering from the University of Pisa, Italy, in 2020. He then pursued a Ph.D. in Electrical and Electronic Engineering at the University of Nottingham, UK, where he is currently a Research Fellow with the Power Electronics, Machines, and Control (PEMC) Research Institute. His primary research interests include the modelling, analysis, and design of electric machines for aerospace and automotive applications, focusing on unconventional topologies such as homopolar synchronous machines and cryogenic motors.

Mauro Di Nardo (M'18) received the M.Sc. (Hons.) degree in electrical engineering from the Polytechnic University of Bari, Italy, in 2012, and the Ph.D. degree in electrical machine design from the University of Nottingham, U.K., in 2017. From 2017 to 2019, he was with the AROL spa leading the R&D team focusing on electrical drives design for mechatronics applications. Between 2019 and 2023, he was with the Power Electronics and Machine Control Group of the University of Nottingham as Research Fellow. He is currently an assistant professor in electrical machine and drives at the Polytechnic University of Bari, Italy. He serves as an Associate Editor for the IEEE Open Journal of Industry Applications and IEEE Transactions on Energy Conversion.

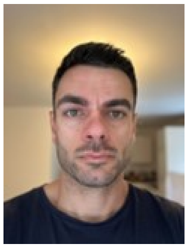

Alessandro Marfoli received the M.Sc. degree in Electrical Engineering from the University of Pisa, Pisa, Italy, in 2015, and the Ph.D. degree in Electrical Machines and Drives from the University of Nottingham, Nottingham, U.K., in 2020. He has worked as a Research Fellow at the University of Nottingham on various projects with significant industrial and scientific impacts. In 2022, he joined Eaton Aerospace as Lead Motor Design Engineer, focusing on electrical machines for actuation in hydraulic and fuel aircraft systems. Since 2024, he has been working at the Arquimea Research Center, where he is developing actuation systems for future robotic systems designed for human interaction. His main research interests include the modeling, analysis, and optimization of asynchronous and synchronous electrical machines, with a focus on unconventional topologies such as multi-phase machines for bearingless applications and high-torque Vernier motors with multiple degrees of freedom.

Jacopo Riccio (Member, IEEE) received the B.Sc. and M.Sc. degrees in mechanical engineering from the University of Roma Tre, Rome, Italy, in 2014 and 2018, respectively. In 2023, he received a Ph.D. degree in electrical engineering from the University of Nottingham, Nottingham, UK. He won the Alessandro Costabeber Award as the best graduating PhD student in 2023 within the Power Electronics, Machine and Control Group. Since 2023, he has been a Research Fellow with the Power Electronics, Machine and Control Group, University of Nottingham, UK. His research interests include the control of electric drives based on model-based predictive control and sensorless algorithms, and experimental characterizations of internal permanent magnet and synchronous reluctance machines for automotive and aerospace applications.

Mukhammed Murataliyev (S'17-M'21) received his Master's degree in electrical engineering from the University of Nottingham, Malaysia, in 2016. He obtained his Ph.D. degree from the University of Nottingham, in 2021, with a focus on novel synchronous reluctance motor design and optimization methods. From 2018 to 2020, he was a Researcher with the Key Laboratory of More Electric Aircraft Technology of Zhejiang Province, China. Since 2021, Dr. Murataliyev has been with the Power Electronics and Machine Control Group at the University of Nottingham, UK, initially as a Research Fellow. In 2023, he was promoted to Senior Research Fellow. His main research interests include the design and modelling of reluctance and permanent magnet machines for industrial and aerospace applications. In addition to his research roles, he currently works as a Lead Electromagnetic Design Engineer at NDSS, DER. He has been involved in a number of technical and industrial consulting projects in the aerospace and automotive sectors, working both part-time and full-time.

Antonino La Rocca received his Ph.D. from the Department of Mechanical, Materials and Manufacturing Engineering Department, University of Nottingham, UK, in 2016. He is a Research Fellow in the Fluids and Thermal Engineering Research Group and the Power Electronics, Machines and Control Research Group in the Faculty of Engineering at the University of Nottingham. His research field is the thermo-mechanical modelling and design of high speed and high power dense electrical machines, power electronics and battery packs for advanced generation and propulsion systems using Lumped Parameters Thermal networks (LPTN) and Computational Fluid Dynamics (CFD) and FEA.

Chris Gerada received the Ph.D. degree in numerical modeling of electrical machines from The University of Nottingham, Nottingham, U.K., in 2005. He was a Researcher with The University of Nottingham, working on high-performance electrical drives and on the design and modeling of electromagnetic actuators for aerospace applications. In 2008, he became a Lecturer in electrical machines, in 2011, as an Associate Professor, and in 2013, a Professor at The University of Nottingham. His main research interests include the design and modeling of high-performance electric drives and machines. He has secured major industrial, European and U.K. grants, authored more than 200 papers and was awarded a Royal Academy of Engineering Research Chair to consolidate research in the field.